*Journal of Advanced Ceramics*
2024, **13**(10): 1611–1621
https://doi.org/10.26599/JAC.2024.9220961

Research Article

# High-pressure synthesis, mechanical properties, and oxidation behavior of advanced boron-containing α/β-$Si_3N_4$/Si ceramics using polymer-derived amorphous SiBN ceramics

Wei Li[2], Shuailing Ma[1,✉], Siwen Cui[3], Jingxue Ding[2], Marc Widenmeyer[2], Xiaoqi Zhang[3], Ying Zhan[2,✉], Zhaoju Yu[5], Wenshu Zhang[1], Pinwen Zhu[3], Tian Cui[1], Anke Weidenkaff[2,4], Ralf Riedel[2]

[1] *Institute of High Pressure Physics, School of Physical Scientific and Technology, Ningbo University, Ningbo 315211, China*
[2] *Department of Materials and Earth Sciences, Technical University of Darmstadt, Darmstadt 64287, Germany*
[3] *Synergetic Extreme Condition High-Pressure Science Center, State Key Laboratory of Superhard Materials, College of Physics, Jilin University, Changchun 130012, China*
[4] *Fraunhofer Research Institution for Materials Recycling and Resource Strategies IWKS, Alzenau 63755, Germany*
[5] *College of Materials, Key Laboratory of High Performance Ceramic Fibers (Xiamen University), Ministry of Education, Xiamen 361005, China*

Received: April 9, 2024; Revised: August 19, 2024; Accepted: August 20, 2024



**Abstract:** The preparation of dense $Si_3N_4$-based ceramics has attracted great attention because of the achievable improvements in their mechanical properties and high-temperature oxidation resistance. In this work, advanced dense boron-containing α/β-$Si_3N_4$/Si monoliths were prepared via a high pressure–high temperature technique in which polymer-derived amorphous SiBN powders were used as raw materials. The crystallization behavior and phase transformation of the polymer-derived amorphous samples were studied in the temperature range from 1400 to 1800 °C. The results demonstrate that the incorporation of boron in the $Si_3N_4$ matrix suppresses the phase transformation from α-$Si_3N_4$ to β-$Si_3N_4$. Furthermore, the mechanical properties of the as-prepared samples were measured, and the maximum hardness and fracture toughness of boron-rich SiBN samples reached 14.8 GPa and 7.96 MPa·$m^{1/2}$, respectively. The hardness of the obtained boron-rich SiBN samples is stable up to 300 °C. In addition, the oxidation behavior of the samples prepared at 1400 and 1600 °C was investigated at 1400 °C for 50 h. The results show that the incorporation of boron significantly improved the oxidation resistance of the samples because of the formation of borosilicate/cristobalite. This work provides guidance for the synthesis of boron-containing α/β-$Si_3N_4$-based ceramics with excellent mechanical properties and oxidation resistance.

**Keywords:** high-pressure synthesis; $Si_3N_4$; mechanical properties; oxidation resistance

## 1 Introduction

Light-element nitride ceramics (e.g., BN and $Si_3N_4$) have been widely applied in structural and technological fields owing to their chemical/thermal stability, low dielectric properties, high thermal conductivity, superior mechanical properties, and outstanding corrosion resistance over a broad range of temperatures [1–5]. However, only a handful of studies have explored the preparation and properties of polycrystalline boron-containing $Si_3N_4$ materials compared with those of $Si_3N_4$- and BN-based composites, which have been extensively studied in the last two decades. Numerous studies have demonstrated that boron results in more dynamic constraints on the migration of Si and N atoms in Si–N ceramic network, resulting in an inhibitory effect on the decomposition of $Si_3N_4$ ceramics as well as improved mechanical properties and high-temperature behavior [6–9]. In general, the densification of nitride ceramic materials is achieved by liquid-phase sintering via oxidic-based sintering additives such as $Al_2O_3$ and $Y_2O_3$ because of their high degree of covalent bonding [10–13]. However, the sintering additives usually remain as crystalline or amorphous phases at grain boundaries and/or at grain junctions. These intergranular phases soften at high temperatures, causing creep and reducing the high-temperature behavior. These features limit the application of nitride ceramics at high temperatures under harsh conditions [14–16]. For example, Wang *et al.* [17] reported that the thermal conductivity of $Si_3N_4$ ceramics obtained by binary nonoxide additives increased by 32% compared to those oxidic sintering additives such as $ZrO_2$–MgO [17]. Recently, the removal and crystallization of the grain boundary glass phase in $Si_3N_4$ ceramics were investigated by Chen *et al.* [4] via post annealing heat treatment. The results show that the flexural strength and thermal conductivity of heat-treated $Si_3N_4$ ceramics increased with increasing the annealing temperature.

In recent years, considerable interest has been developed in the preparation of additive-free $Si_3N_4$-based ceramics. β-$Si_3N_4$ monoliths with high relative density (≥ 99%) were first prepared without the use of sintering additives by hot isostatic pressing (HIP) above 1900 °C [18]. The resultant dense β-$Si_3N_4$ materials

✉ Corresponding authors.
E-mail: S. Ma, mashuailing@nbu.edu.cn;
Y. Zhan, ying.zhan@tu-darmstadt.de

exhibit outstanding mechanical properties even at high temperatures, and Vickers hardness of 13.2 GPa and flexural strength of 750 MPa are achieved at 1300 and 1400 °C, respectively. The feasibility of densifying high-purity α-$Si_3N_4$ without the use of sintering aids was studied by Tanaka *et al.* [19,20], and the obtained samples exhibited improved mechanical properties compared with those of samples prepared with sintering additives. However, all of these consolidations are strongly dependent on the presence of $SiO_2$ on the surface of $Si_3N_4$ powder particles under high sintering temperatures of up to 1950 °C, and long holding time. Furthermore, the transformation from α-$Si_3N_4$ to β-$Si_3N_4$ and grain growth occur uncontrollably because of the high sintering temperature. Therefore, it is still a challenge to synthesize fine-grained α-$Si_3N_4$ or α-/β-$Si_3N_4$ bodies with high hardness via conventional pressure sintering methods. Lu *et al.* [21] reported that dense and additive-free β-$Si_3N_4$ ceramics can be prepared via HIP using amorphous $Si_3N_4$ as starting material. Compared with crystalline materials, amorphous materials possess a much more disordered structure, highly homogeneous sites down to the atomic scale, composition flexibility, isotropic molecular diffusion, and more percolation pathways in solid mixtures, providing more densification possibilities. Polymer-derived ceramic (PDC) route is an attractive method for the fabrication of amorphous ceramics because of the facile tailoring of the element content at the molecular level, which has significant advantages over traditional ceramic processing techniques [22–24].

Pressure, like temperature, is a fundamental thermodynamic variable and has a significant effect on material synthesis. High pressure can induce atomic planes to coincide along small-angle grain boundaries because of plastic deformation, which has a significant effect on particle redistribution, pore elimination, and destruction of agglomerates [25,26]. Furthermore, high-pressure sintering can dramatically reduce the sintering temperature and, to some extent, suppress decomposition, phase transformation, and excessive grain coarsening, effectively increasing the density and mechanical properties [22,27,28]. For example, additive-free $B_4C$/SiC ceramic composites were densified at 1500 °C under high pressure of 4 GPa for 60 s [28]. The relative density of the resulting $B_4C$/SiC composite is similar to that of a sample prepared by pressureless sintering using sintering additives at 2100 °C [29]. Furthermore, the obtained sample exhibited a high Vickers hardness of 31 GPa and good thermal conductivity at 1000 °C. Another example is the preparation of dense β-$Si_3N_4$ compacts without sintering additives at a pressure of 5.5 GPa [30]. The fracture toughness of the obtained sample reaches 4.1±0.3 MPa·$m^{1/2}$, which is 36% greater than that of conventional additive-free β-$Si_3N_4$ monoliths (~3 MPa·$m^{1/2}$). The aforementioned examples clearly demonstrate that high pressure is an effective method to fabricate highly dense covalent ceramics without sintering additives, which has attracted significant interest in recent years [31–33].

To gain a better understanding of the high-pressure sintering potential for the consolidation of strong covalent compounds derived from amorphous precursors, the fabrication of boron-containing dense α/β-$Si_3N_4$ ceramics at a pressure of 5 GPa is presented in the current work. Polymer-derived amorphous SiBN ceramic powders are synthesized and used as starting materials for high-pressure densification. The influences of boron content and sintering temperature on phase evolution, mechanical properties, and oxidation resistance of the prepared samples are systematically characterized and discussed.

## 2 Materials and methods

### 2.1 Experimental

Perhydropolysilazane (PHPS)- and boron-modified PHPS (BPHPS)-derived ceramic powders were prepared via PDC route, and the detailed single-source-precursor (SSP) synthesis and heat-treatment procedures can be found in our previous work [34]. Similarly, the boron-containing SSPs were synthesized upon reacting a commercially available PHPS solution (20 wt% of PHPS in dibutyl ether, Merck KGaA, Germany) with borane dimethyl sulfide complex (BMS; Sigma–Aldrich, Germany). Si/B molar ratios of the synthesized SSPs were set to 1, 2, and 5. The obtained BPHPS precursors were subsequently ground and pyrolyzed at 1100 °C under a constant flow of $N_2$ for 2 h. The resulting amorphous SiBN samples with Si:B molar ratios of 5, 2, and 1 are denoted as SiBN5, SiBN2, and SiBN1, respectively. X-ray diffraction (XRD) patterns of the pyrolyzed PHPS- and BPHPS-precursor are shown in Fig. 1. The chemical composition of the raw materials was measured and is shown in Table 2. The as-obtained powders were milled in a $ZrO_2$ jar under an argon atmosphere via high-energy ball milling (1800 r/min) for 3 h and then sieved through two sieves (180 and 100 μm sieves, Merck, Germany) to obtain fine powders for the subsequent high-pressure experiments (Fig. S1 in the Electronic supplementary material (ESM)). The starting materials were prepressed into bulk materials (4 mm in diameter and 2.5 mm in height) via a hydraulic press. To prevent reactions between the sample and surrounding materials, hexagonal boron nitride was used to insulate the sample from the graphite heater. High-pressure and high-temperature sintering experiments were conducted with a China-type SPD 6′600T cubic press at Jilin University. Six anvils applied forces to the sample from six sides simultaneously to avoid grain orientation. The pressure was determined in advance by the phase transformation of Bi, Tl, and Ba. The temperature of the high-pressure chamber was calibrated with a C-type thermocouple with a temperature uncertainty of ~20 °C. When the pressure reached 5 GPa, the samples were heated to temperatures of 1400, 1600, and 1800 °C and held for 20 min. After pressure release, the sample was quenched and cooled to room temperature. A macro photograph of the obtained monoliths prepared at 1600 °C is shown in Fig. S1 in the ESM.

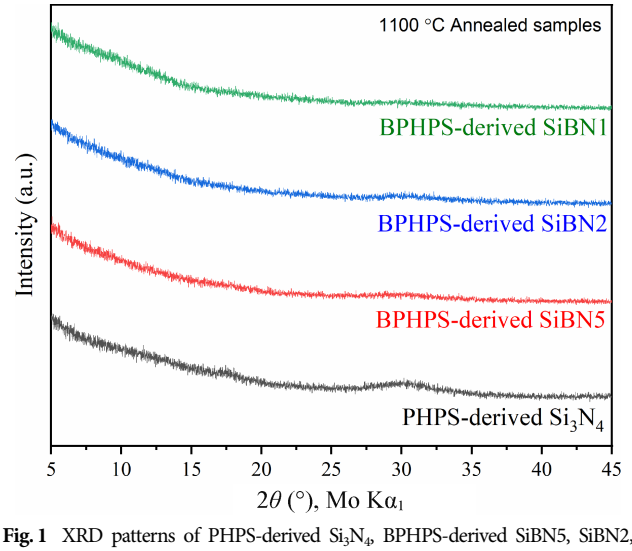


**Fig. 1** XRD patterns of PHPS-derived $Si_3N_4$, BPHPS-derived SiBN5, SiBN2, and SiBN1 samples pyrolyzed at 1100 °C in nitrogen atmosphere.

The quenched body was polished to conduct the subsequent measurements. The samples prepared at different temperatures are denoted as SiBN*X*-temperature. For example, SiBN1-1600 represents SiBN sample with a molar ratio of Si : B = 1 : 1, which was prepared at 1600 °C.

## 2.2 Characterizations

The phase identification of the recovered samples was performed via a Cu $K\alpha_1$ XRD (D/Max-2500, Rigaku, Japan) in reflection geometry at a scan rate of 2 (°)/min. XRD patterns of the samples oxidized at 1400 °C and in different directions were obtained on a STADI P XRD diffractometer using Mo $K\alpha_1$ radiation source (STOE & Cie GmbH, Germany) in transmission geometry. The as-prepared high-pressure samples were sputter coated with gold for characterization of their microstructure and chemical composition via a scanning electron microscope (SEM; 30 kV, JSM 7600F, JEOL Ltd., Japan) equipped with an energy-dispersive detector (EDS). Transmission electron microscopy (TEM) measurements were performed with a microscope (JEM-2100, JEOL Ltd., Japan), and the acceleration voltage was 200 kV. Thin SiBN1 sample was prepared via the focused ion beam (FIB) technique (EM-F200, JEOL Ltd., Japan) and used for TEM observation. The boron and silicon contents of the pyrolyzed samples were detected via inductively coupled plasma–atomic emission spectrometry (ICP–AES) at Mikroanalytisches Labor Pascher (Remagen, Germany). The nitrogen and oxygen contents of the samples were measured via thermal conductivity and infrared (IR) analysis, respectively. Thermal conductivity for nitrogen was measured by changes in the base gas composition, resulting in changes in the filament resistance. Nitrogen in a sample will cause such changes and will be recorded as an analytical signal. Oxygen present in the sample reacts with the graphite crucible to form CO and $CO_2$, which are detected via nondispersive infrared cells. Carbon analysis was carried out with an analyzer (LECO C-200, LECO Co., USA) in our laboratory.

The recovered high-pressure samples were polished with 1/4 mm polycrystalline diamond on felt cloth for density, mechanical property, and oxidation resistance measurements. The bulk density and open porosity of the as-recovered monoliths were measured via the water immersion method (Archimedes' method). Vickers hardness measurements were performed on a microindenter system (AHVD-1000XY, HMAS-D2000SMZC, China) with a pyramid-like diamond Vickers indenter under a load of 9.8 N held for 15 s, and at least five arbitrary measurements were repeated to ensure reliability. The fracture toughness was calculated from the indentation crack ($c$) and impression diagonal ($a$) using the Evans equation (Eq. (1)) [22,35]:

$$K_{\text{IC-Evans}} = 0.16 \times H_v \times a^2/c^{1.5} \quad (1)$$

where $K_{\text{IC-Evans}}$ is fracture toughness, $H_v$ is Vicker's hardness, $c$ represents the indentation crack, and $a$ is the impression diagonal. The oxidation experiments were performed in a muffle furnace (Glüh- und Härteöfen, Arnold Schröder Industrieöfen GmbH, Germany) under air conditions. The oxidation procedures were as follows: First, the furnace was heated to 1400 °C and held for 30 min; subsequently, the samples for oxidation were placed in the isothermal area of the furnace, and their weights were recorded after dwelling times of 1, 2, 3, 5, 10, 20, 30, 40, and 50 h. At least five weight measurements were repeated and averaged to ensure the reliability of the results.

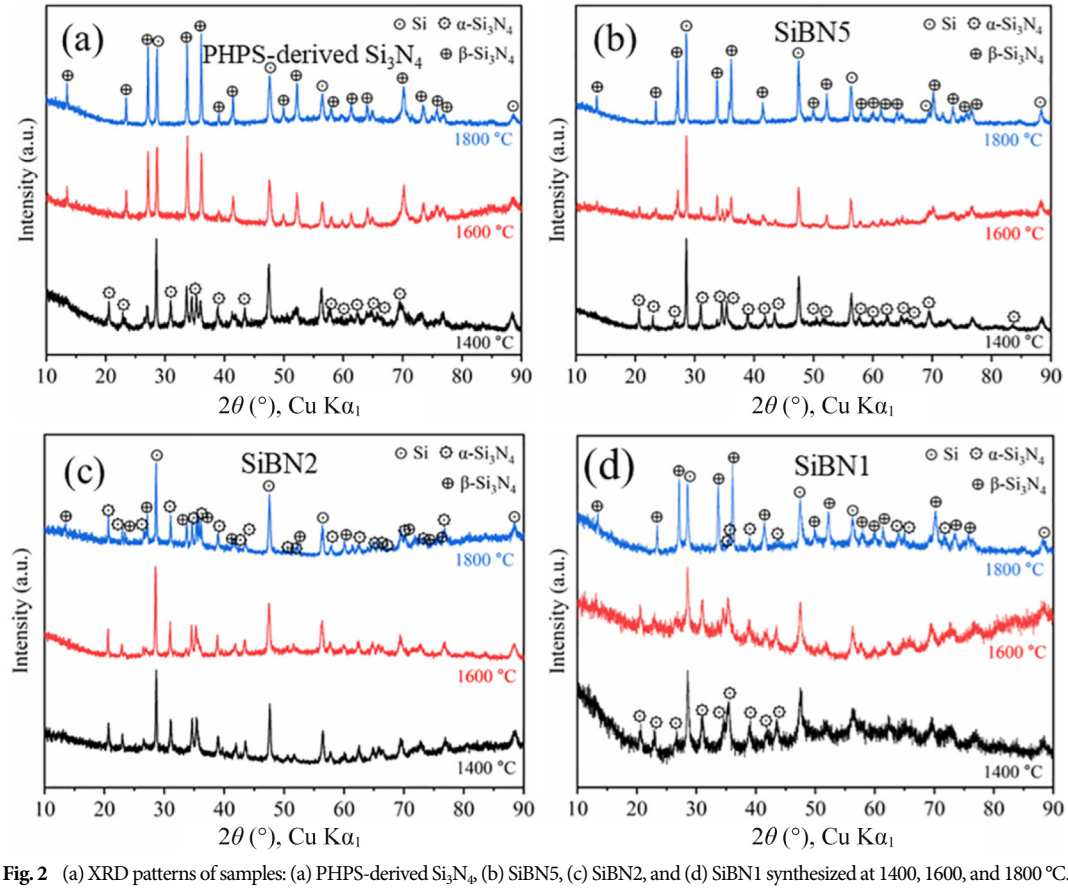


**Fig. 2** (a) XRD patterns of samples: (a) PHPS-derived $Si_3N_4$, (b) SiBN5, (c) SiBN2, and (d) SiBN1 synthesized at 1400, 1600, and 1800 °C.

## 3 Results and discussion

### 3.1 Crystallization and microstructural evolution

Figure 2 and Fig. S2 in the ESM show XRD patterns of $Si_3N_4$ and SiBN samples prepared at 5 GPa and temperatures ranging from 1400 to 1800 °C. As shown in Fig. 2, silicon and α-$Si_3N_4$ were the main phases present at 1400 °C in all recovered samples. As the sintering temperature increased to 1600 °C, a significant effect of boron on crystallization was observed. To confirm the phase composition of the samples prepared at 1600 °C, a quantitative phase analysis was carried out by Rietveld refinements using the GSAS II software, and the Rietveld patterns and weight fractions are shown in Table 1 and Fig. S2 in the ESM, respectively. The complete phase transformation from α-$Si_3N_4$ to β-$Si_3N_4$ clearly occurs in the boron-free $Si_3N_4$ sample, whereas the phase transformation is hindered with increasing boron content in SiBN-1600 samples. As shown in Fig. 2 and Fig. S2 in the ESM, some low-intensity reflections of α-$Si_3N_4$ are identified in SiBN5-1600 sample, whereas α-$Si_3N_4$ appears to be the major phase in SiBN2-1600 and SiBN1-1600 samples. The strongest reflections of β-$Si_3N_4$ are visible with tiny intensities. From the PHPS-derived $Si_3N_4$ sample to the SiBN1 sample, the weight percentage of α-$Si_3N_4$ increases from 0 to 64.1 wt% (Table 1), whereas the weight fraction of β-$Si_3N_4$ decreases from 69.1 to 9.8 wt%, indicating that the incorporation of boron into Si–N network hinders the transformation from α-$Si_3N_4$ to β-$Si_3N_4$. Notably, samples prepared at 1600 °C present approximately 30 wt% silicon according to the quantitative phase analysis, which is consistent with the results of the elemental analyses (Table 2). PHPS-derived SiN*x* ceramics exhibit ~20 wt% excess silicon [36], although the pyrolysis of PHPS and BPHPS was performed at 1100 °C in a nitrogen atmosphere [34]. Here, an additional 10 wt% excessive silicon exists in the sample, indicating that part of Si, N, and B present as amorphous SiBN, which is confirmed by the broad and low-intensity reflections in XRD patterns.

As the temperature further increases to 1800 °C, XRD patterns of SiBN5-1800 are similar to those of boron-free $Si_3N_4$; β-$Si_3N_4$ is the dominant phase, whereas α-$Si_3N_4$ reflections still remain in SiBN2-1800 and SiBN1-1800 samples. Furthermore, as clearly shown in Fig. 2(d), the reflections of SiBN1-1800 are relatively broad and low in intensity compared with those of other samples, indicating poor crystallization due to the high boron content. These findings demonstrate that the incorporation of boron into Si–N network has a significant effect on the crystallization of PHPS-derived $Si_3N_4$ ceramics (i.e., the higher the boron content is, the lower the degree of crystallization), which is attributed to the formation of the ternary Si–B–N network. Numerous experimental and theoretical studies have proven that the atomic diffusivity of nitrogen and silicon atoms in a network decreases due to the presence of boron in Si–N networks [6,34,37]. Additionally, the grain orientation of the obtained samples was confirmed via XRD, as shown in Fig. S3 in the ESM. XRD diffraction peaks of all samples measured at the same temperature and in different directions are identical, with no observed changes in peak shape or position, indicating the absence of grain orientation in HPHT-derived samples. SEM and TEM observations in the next section further support this conclusion, which is attributed to the six-sided cubic apparatus applying pressure simultaneously from all sides.

The microstructural features of the as-prepared $Si_3N_4$ and SiBN1 samples were further investigated via high-resolution TEM (HRTEM) along with selected area electron diffraction (SAED), as shown in Fig. 3. HRTEM image of PHPS-derived ceramics at 1600 °C reveals a typical crystal structure with lattice spacings of 0.32 and 0.27 nm, corresponding to *d*-spacings of Si(111) and β-$Si_3N_4$(101) lattice planes. Furthermore, SAED patterns (the inset of Fig. 3(a)) also show diffraction spots of Si and β-$Si_3N_4$, which is consistent with XRD results. It is well known that the phase transformation from α → β-$Si_3N_4$ usually takes place at ~1650 °C and is essentially completed at ~1750 °C [38,39]. Herein, complete transformation was already observed via XRD and TEM at 1600 °C, indicating that high-pressure conditions can accelerate the phase transformation from α → β-$Si_3N_4$. HRTEM images of SiBN1-1600 sample prepared under the same condition exhibit α-$Si_3N_4$ lattice plane exclusively. Although no β-$Si_3N_4$ crystallites are visualized in HRTEM images, the diffraction spots of β-$Si_3N_4$ are found in SAED pattern, demonstrating that the phase transformation from α → β-$Si_3N_4$ in SiBN1 sample starts at 1600 °C. At 1800 °C, β-$Si_3N_4$ was identified as the main phase (Fig. 3(d)). Interestingly, α-$Si_3N_4$

**Table 1** Weight fractions calculated from Rietveld refinement of samples annealed at 1600 °C

| Crystalline phase (wt%) | $Si_3N_4$ ($R_{wp}$ = 4.152%) | SiBN5 ($R_{wp}$ = 4.851%) | SiBN2 ($R_{wp}$ = 4.869%) | SiBN1 ($R_{wp}$ = 6.578%) |
|---|---|---|---|---|
| α-$Si_3N_4$ | 0.0 | 24.9 | 59.5 | 64.1 |
| β-$Si_3N_4$ | 69.1 | 44.0 | 10.6 | 9.8 |
| Si | 30.9 | 31.1 | 29.9 | 30.8 |

**Table 2** Elemental composition of samples prepared at 1600 °C

| Sample | Composition (wt%) | | | | | Empirical formula |
|---|---|---|---|---|---|---|
| | Si | B | N | C | O | |
| SiN-1100 | 72.14 | 0.00 | 25.83 | 1.01 | 1.02 | $Si_{1.00}N_{0.72}(C_{0.033}O_{0.025})$ |
| SiBN5-1100 | 69.48 | 1.67 | 25.00 | 2.23 | 1.61 | $Si_{1.00}B_{0.06}N_{0.72}(C_{0.075}O_{0.041})$ |
| SiBN2-1100 | 68.50 | 2.56 | 23.00 | 3.36 | 1.36 | $Si_{1.00}B_{0.10}N_{0.67}(C_{0.11}O_{0.04})$ |
| SiBN1-1100 | 66.73 | 4.94 | 24.41 | 2.64 | 1.29 | $Si_{1.00}B_{0.19}N_{0.73}(C_{0.11}O_{0.034})$ |
| SiN-1600 | 71.65 | 0.00 | 26.95 | < LOD | 1.27 | $Si_{1.00}N_{0.75}O_{0.03}$ |
| SiBN5-1600 | 70.87 | 1.43 | 25.00 | < LOD | 1.53 | $Si_{1.00}B_{0.05}N_{0.74}O_{0.04}$ |
| SiBN2-1600 | 69.85 | 2.43 | 23.00 | < LOD | 1.68 | $Si_{1.00}B_{0.10}N_{0.74}O_{0.04}$ |
| SiBN1-1600 | 67.41 | 4.50 | 24.41 | < LOD | 1.69 | $Si_{1.00}B_{0.17}N_{0.78}O_{0.034}$ |

Note: LOD means a limit of detection.

and Si are also visible from HRTEM and SAED results discussed above, indicating that the phase transformation from α → β-$Si_3N_4$ is strongly suppressed due to the presence of boron in $Si_3N_4$ matrix. As mentioned above, the atomic diffusivity of nitrogen and silicon atoms decreases due to the presence of boron in Si–N networks. Moreover, numerous studies have demonstrated that the driving force for α → β-$Si_3N_4$ phase transformation is the formation of a metastable solid solution by the present oxide additive [40,41], which leads to the dissolution of oxidated impurities into α-$Si_3N_4$ crystal lattice. Therefore, additive-free sintering in this work suppresses the phase transformation from α → β-$Si_3N_4$.

### 3.2 Density and mechanical properties

The density, open porosity, and mechanical properties of $Si_3N_4$ and various SiBN ceramics prepared at different temperatures were analyzed, as shown in Table 3 and Fig. 5. Although all the samples were densified with less than 2% open porosity (Table 3), the skeleton density of the obtained samples (between 2.81 and 2.85 g/cm³) was lower than the theoretical density of $Si_3N_4$ ceramics (3.2 g/cm³) [42], which was attributed to the presence of low-density silicon (2.3 g/cm³). Interestingly, the samples prepared at 1600 °C presented the highest skeleton density, indicating that the densification of the samples improved from 1400 to 1600 °C. With increasing temperature up to 1800 °C, the decrease in the skeleton density is attributed to the decomposition of $Si_3N_4$ ceramics during HPHT experiment [43], leading to the formation of pores. Batha and Whitney [43] confirmed that the fractional decomposition of $Si_3N_4$ ceramics at 1675 °C in vacuum is approximately 20 wt%. Notably, the variations in density and open porosity are within the margin of their error, indicating that high pressure not only promotes densification but also suppresses the decomposition of $Si_3N_4$-based ceramics. The morphologies of the synthesized samples were further characterized via SEM to assess the evolution of pores, grain growth, and microstructure at different temperatures. As shown in Fig. 4, no obvious pores are observed, and all the samples have a dense structure, which is consistent with the density results.

Notably, the influence of silicon on the mechanical properties is negligible because all the samples contain the same content of silicon. In addition, on the basis of XRD and TEM results, the effect of temperature is related mainly to the phase composition of

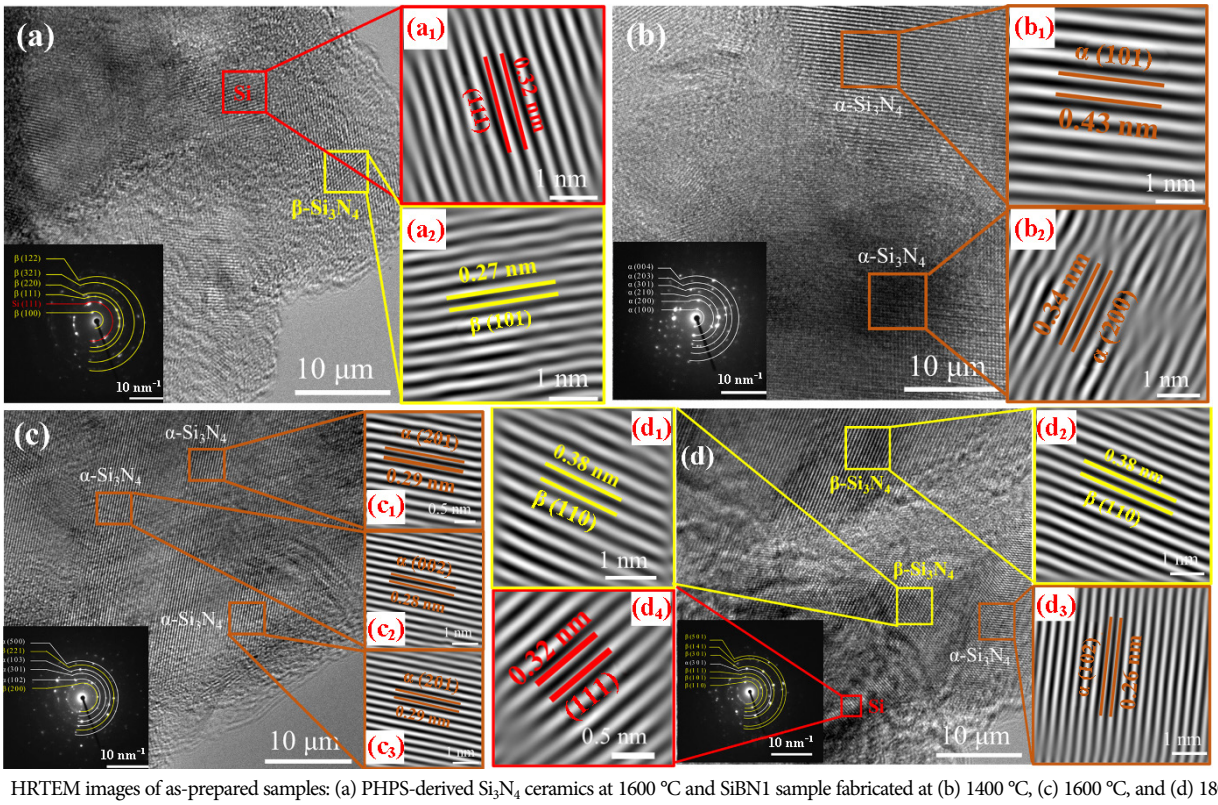


**Fig. 3** HRTEM images of as-prepared samples: (a) PHPS-derived $Si_3N_4$ ceramics at 1600 °C and SiBN1 sample fabricated at (b) 1400 °C, (c) 1600 °C, and (d) 1800 °C. Images on the left and right of (a–d) are FFT images of selected areas; the insets in (a–d) are SAED images.

**Table 3** Density and open porosity of $Si_3N_4$ and SiBN ceramics prepared at 1400, 1600, and 1800 °C

| | Sample | 1400 °C | 1600 °C | 1800 °C |
|---|---|---|---|---|
| Density (g/cm³) | $Si_3N_4$ | 2.830±0.019 | 2.850±0.026 | 2.812±0.022 |
| | SiBN5 | 2.824±0.021 | 2.852±0.029 | 2.811±0.030 |
| | SiBN2 | 2.816±0.041 | 2.841±0.041 | 2.814±0.048 |
| | SiBN1 | 2.829±0.022 | 2.852±0.029 | 2.817±0.036 |
| Porosity (%) | SiN | 0.383±0.007 | 0.521±0.009 | 0.457±0.008 |
| | SiBN5 | 0.427±0.007 | 0.575±0.010 | 1.201±0.010 |
| | SiBN2 | 1.646±0.014 | 1.701±0.013 | 1.934±0.018 |
| | SiBN1 | 0.973±0.008 | 1.059±0.009 | 1.434±0.012 |

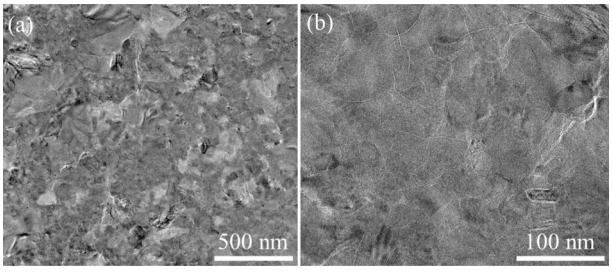


**Fig. 4** TEM micrographs of SiBN1 sample fabricated at 1600 °C.

the samples, which is considered to be the critical factor affecting the mechanical properties. As shown in Fig. 5, the samples obtained at 1400 °C exhibited the highest Vickers hardness compared with the samples fabricated at 1600 and 1800 °C. The theoretical hardness of α-$Si_3N_4$ ceramics (21 GPa) is greater than that of β-$Si_3N_4$ ceramics (16 GPa) [44], and the main phase at 1400 °C is α-$Si_3N_4$, thus leading to the highest hardness. This conclusion is further confirmed by the hardness results of the samples prepared at 1600 and 1800 °C, and a comparison between them can be seen in Fig. 5. Vickers hardness of SiBN samples obtained at 1600 °C was greater than that of the samples prepared at 1800 °C. As demonstrated by XRD and TEM results, SiBN-1600 samples were composed of α-$Si_3N_4$ and β-$Si_3N_4$, whereas α-$Si_3N_4$ completely transferred into β-$Si_3N_4$ in SiBN-1800. In addition, the lower hardness of SiBN samples prepared at 1800 °C is related to the presence of h-BN (the Vickers hardness is ca. 0.8 GPa) [45]. h-BN phase separates from the amorphous SiBN phase at 1800 °C [46], but it was not distinguished from XRD and TEM results because of its weak crystal quality and inhomogeneous distribution, which was also reported by Baldus and Passing [47] and Kaur *et al.* [48].

In addition to the temperature, the boron content has a significant effect on hardness. Vickers hardness of $Si_3N_4$ samples is clearly greater than that of SiBN5 samples but lower than that of SiBN1 and SiBN2 samples. The $Si_3N_4$ and SiBN5 samples have similar phase compositions. Therefore, the slight decrease in the hardness of SiBN5 monoliths is related to the density of the samples. The lower density of SiBN5 sample is explained by the formation of a rigid Si–B–N network [49], which obviously densifies differently from that of the boron-free sample. The relatively high open porosity (Table 3) also results in a reduced hardness compared with that of $Si_3N_4$ samples. As shown in Fig. 5(a), increasing the boron content in SiBN2 and SiBN1 leads to increasing hardness due predominantly to the presence of α-$Si_3N_4$. Notably, the hardness of the obtained samples is not as high as that of $Si_3N_4$ prepared with sintering additives (~17 GPa) [50,51] because of the presence of ~30 wt% Si (~11 GPa) [52]. Furthermore, Vickers hardness of SBN1 samples prepared at different temperatures was also characterized from room temperature to 300 °C (Fig. 5(b)). Vickers hardness of SBN1 samples is stable, indicating a relatively stable hardness below 300 °C.

Fracture mechanics studies have shown that the results are closely related to the phase content of elongated β-$Si_3N_4$ and the coarsened bimodal microstructure [53,54]. In the present study, the fracture toughness did not increase significantly with increasing β-$Si_3N_4$ content (Table 1 and Fig. 5(a)). In contrast, it shows a decreasing trend in the SiBN1 sample. This phenomenon is attributed to the grain size effect. The grain sizes and morphologies of the obtained samples were characterized via TEM (Fig. 4) and SEM (Fig. S4 in the ESM). The average grain size of the SBN1 and SiBN2 samples was as low as 150 nm even for the samples prepared at 1800 °C, whereas the grain sizes of $Si_3N_4$ and SiBN5 samples reached 500 nm, indicating that the presence of boron prevents grain growth due to the formation of a rigid Si–B–N network. Additionally, with increasing boron content, elongated β-$Si_3N_4$ grains do not develop, and the grain size further decreases (~150 nm). Therefore, the effects of elongated β-$Si_3N_4$ and coarsened bimodal microstructures are negligible. In addition to the effect of boron on grain growth, high pressures up to 5 GPa also suppress grain growth. The variation in fracture toughness is considered to be related to the presence of boron. On the one hand, disordered SiBN boundary phases play an important role in improving the plasticity of $Si_3N_4$ ceramics by acting as lubricants to enhance grain boundary sliding [22]. On the other hand, the soft h-BN phase separated from the amorphous SiBN phase can also act as a lubricant to promote grain boundary deformation [46], thereby leading to improved fracture toughness in the SiBN samples.

To comprehensively assess the mechanical properties of the boron-containing $Si_3N_4$ ceramics, a comparison with reported $Si_3N_4$-based materials is compiled and shown in Fig. 6 [53,55–64]. The SiBN1-derived $Si_3N_4$ samples clearly have higher fracture toughness values than most of the reported $Si_3N_4$-based materials do without sacrificing hardness, even when 30 wt% low-hardness Si (~11 GPa) is included. Accordingly, the resulting $Si_{1.00}B_{0.17}N_{0.78}O_{0.034}$ ceramic possesses both high hardness and fracture toughness. Therefore, boron-containing $Si_3N_4$ ceramics prepared via a high-pressure technique are considered potential candidate materials for structural applications.

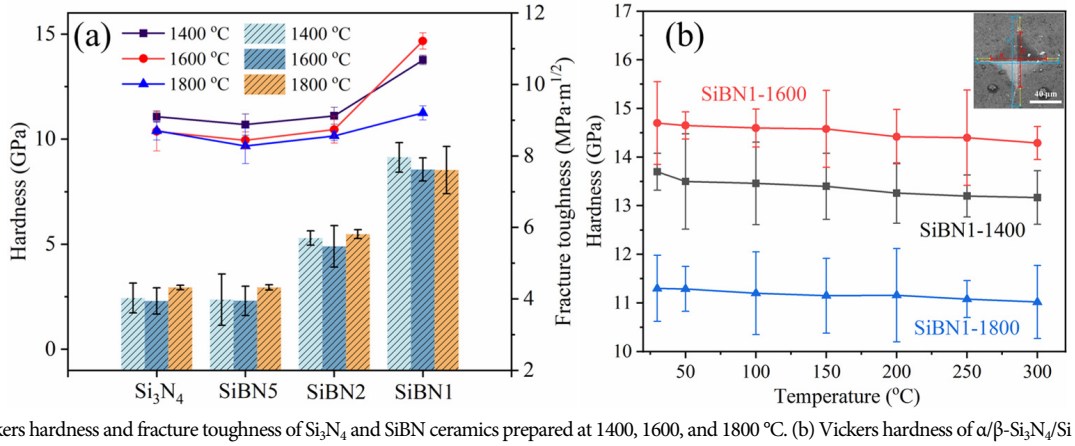


**Fig. 5** (a) Vickers hardness and fracture toughness of $Si_3N_4$ and SiBN ceramics prepared at 1400, 1600, and 1800 °C. (b) Vickers hardness of α/β-$Si_3N_4$/Si as a function of temperature in the range of room temperature to 300 °C (detailed values are shown in Table S1 in the ESM). The inset is representative SEM indentation image showing cracks under indentation load of 9.8 N.

### 3.3 Oxidation behavior

The isothermal oxidation resistance of SiBN-1400 and SiBN-1600 samples was investigated in air at a temperature of 1400 °C. SiBN1 samples oxidized at 1400 °C for 1 h are partially covered by glass-like oxidation products with large and nearly bursting bubbles, as shown in Fig. S5 in the ESM. The transparent oxidation products are low-melting-point borosilicate glasses formed by the reaction of $SiO_2$ and $B_2O_3$ due to the excessive boron content, which evaporates at the oxidation temperature [65,66], resulting in a heavily damaged surface (Fig. S4 in the ESM). Therefore, the mass change of SiBN1 was not recorded because of extensive damage to the samples. The isothermal oxidation curves of $Si_3N_4$, SiBN5, and SIBN2 samples oxidized at 1400 °C are shown in Fig. 7. The mass change of the obtained samples is smaller than that of most reported SiBN-related ceramics, such as SiBCN [67], SiCN [68], SiBN [69], and $Si_3N_4$ [70], indicating good oxidation resistance. SiBN samples exhibited a mass loss in the first hour and then a gradual increase until stabilization after 10 h of oxidation, indicating parabolic oxidation behavior. However, $Si_3N_4$ ceramics deviate from pure parabolic behavior with increasing oxidation time, which is similar to the behavior of CVD-synthesized $Si_3N_4$ [71]. The mass change in the initial stage is attributed to the oxidation of the segregated carbon with a weight fraction of ca. 1.5 wt% [34]. In SiBN samples, the mass change is also related to the evaporation of liquid $B_2O_3$. The mass loss due to the presence of boron is stabilized by the formation of borosilicate glass with $SiO_2$ [72]. These results indicate that the SiBN sample with a boron content of ~0.05 mol% has improved oxidation resistance compared with that of the boron-free $Si_3N_4$ at 1400 °C. Excessive boron leads to significant volatilization of $B_2O_3$ gas at high temperatures, which is consistent with the results reported by Long *et al.* [73].

To investigate the influence of boron on the oxidation behavior of SiBN and $Si_3N_4$ ceramics and assess the evolution of the surface during oxidation, the oxidized samples were characterized via XRD (Fig. 8 and Fig. S6 in the ESM) and SEM (Fig. 9 and Fig. S7 in the ESM). As shown in Fig. 8, α/β-$Si_3N_4$ and small amounts of cristobalite ($SiO_2$) were detected as the main phases after oxidation, indicating that cristobalite dominated the oxidation phases of SiBN and $Si_3N_4$ monoliths. This behavior is in line with various studies related to the high-temperature oxidation of $Si_3N_4$ ceramics [71,74,75]. The results reveal that the diffusion of oxygen through the cristobalite layer is the rate-controlling step, ultimately resulting in parabolic oxidation kinetics. However, no signals related to boron-containing crystalline phases are detected via XRD. As mentioned previously, $B_2O_3$ is preferentially depleted at high temperatures because of its low melting point [72,76], which continuously decreases the amount of boron. In addition, published studies have shown that the formed $B_2O_3$ easily dissolves in $SiO_2$ above ~900 °C to form borosilicate glass [67,77], which cannot be detected by XRD.

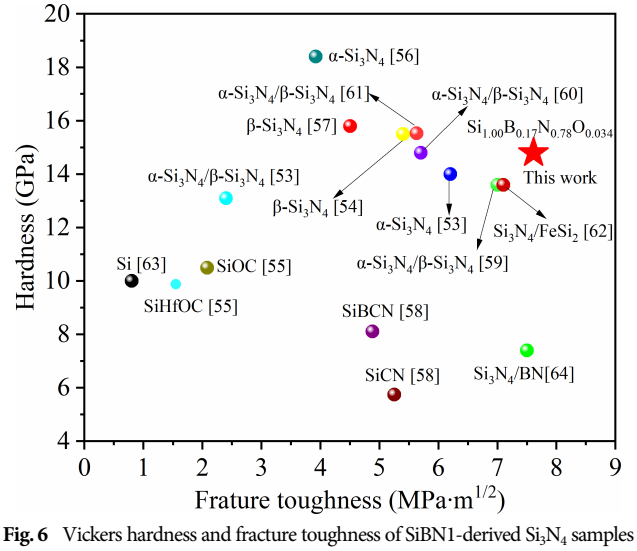


**Fig. 6** Vickers hardness and fracture toughness of SiBN1-derived $Si_3N_4$ samples (load: 9.8 N) in comparison with those of similar reported materials.

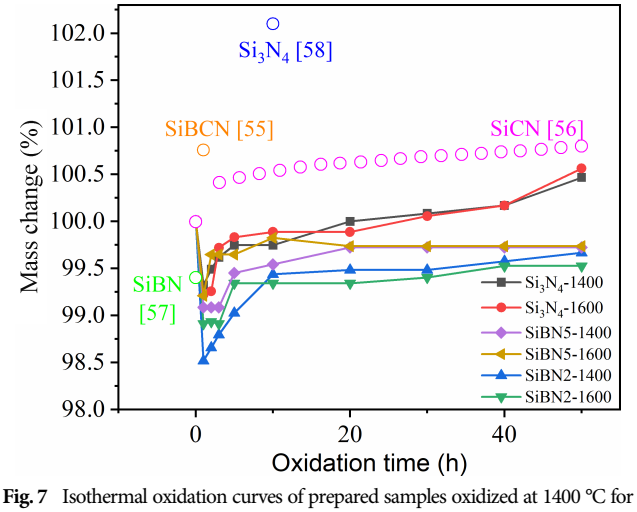


**Fig. 7** Isothermal oxidation curves of prepared samples oxidized at 1400 °C for 50 h in air.

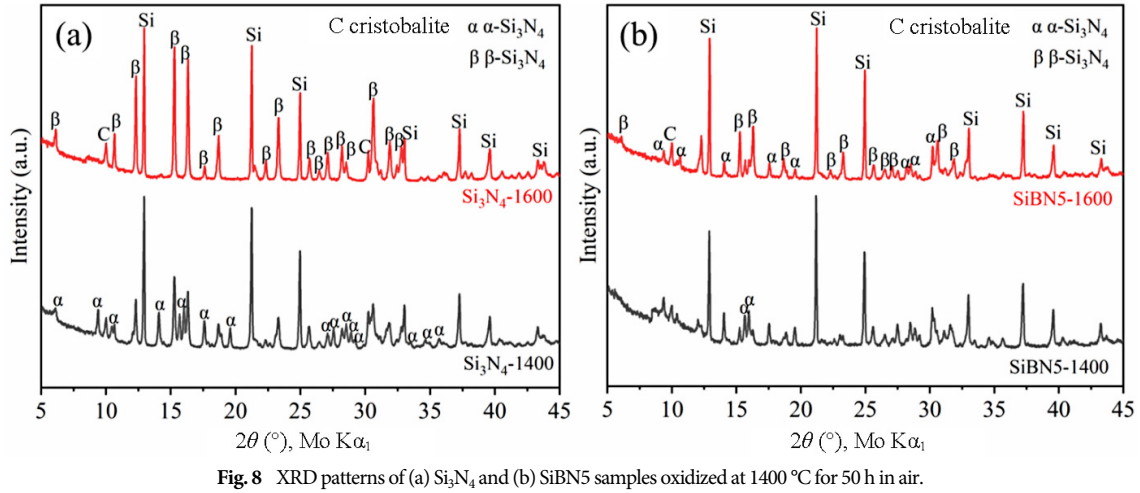


**Fig. 8** XRD patterns of (a) $Si_3N_4$ and (b) SiBN5 samples oxidized at 1400 °C for 50 h in air.

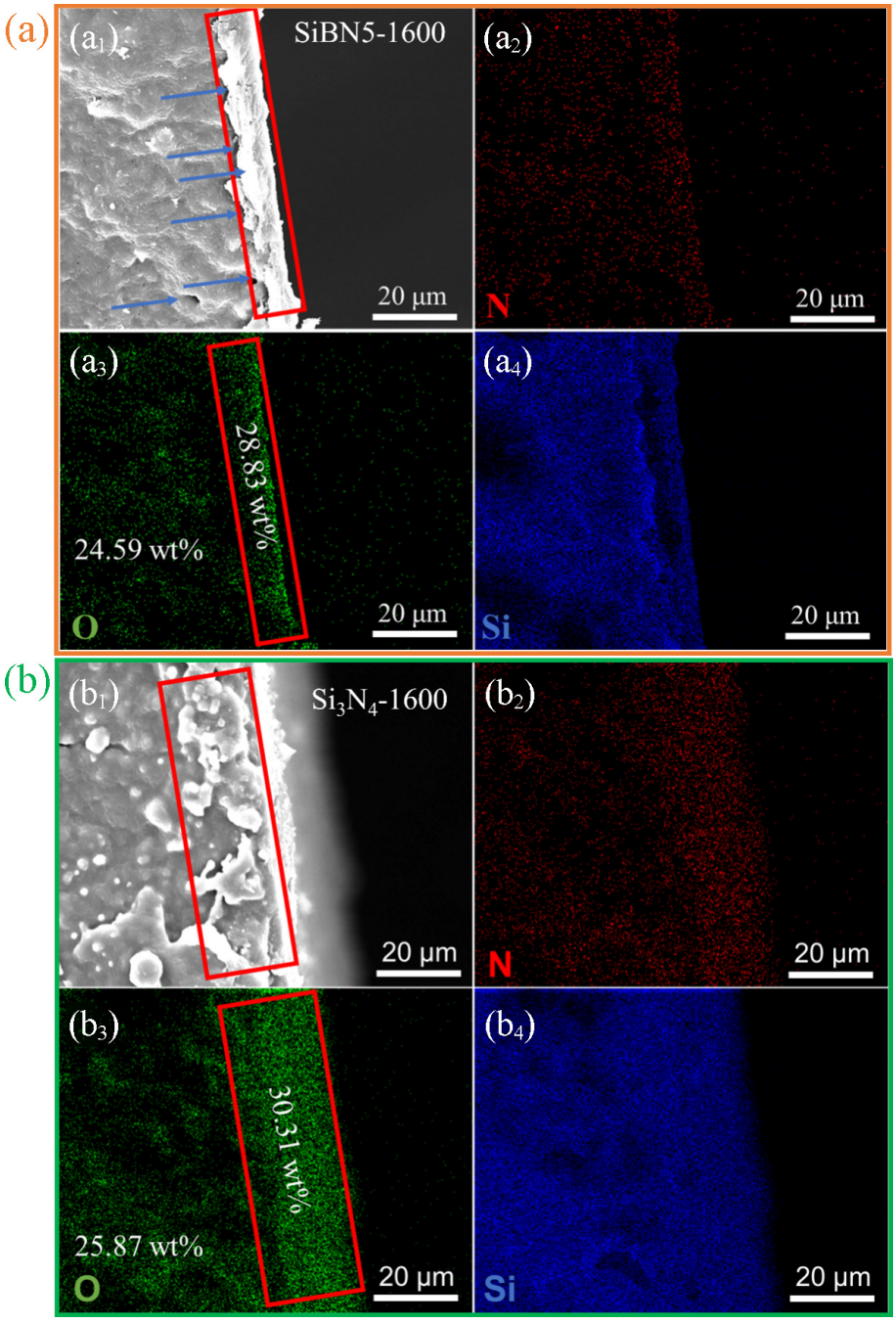


**Fig. 9** SEM images and EDS mappings of cross sections of (a) SiBN5-1600 and (b) $Si_3N_4$-1600. Sample was exposed to 1400 °C in air. Red box illustrates oxide scale. Blue arrows indicate pores produced by evaporation of boron and outward diffusion of gaseous species.

The cross-sections of the samples oxidized at 1400 °C were characterized via SEM/EDS, as shown in Fig. 9 and Fig. S6 in the ESM. SEM images of the SiBN5-1600 and SiBN2-1600 samples (Fig. 9(a) and Fig. S7 in the ESM) show an oxide scale at the surface comparable with that of $Si_3N_4$-1600 (Fig. 9(b)). The oxide scale thickness of the $Si_3N_4$-1600 sample can be determined via EDS mappings, especially the distribution of oxygen, which is between 25 and 30 μm and is much greater than that of the SiBN-1600 sample (~15 μm). The oxide scale thickness of the SiBN5-1600 samples is comparable to that of CVD-synthesized $Si_3N_4$ oxidized at 1400 °C for 8 h, indicating improved oxidation resistance [78]. Furthermore, the oxygen content was also measured, as shown in the corresponding EDS mappings. The results show that the oxygen content of the $Si_3N_4$-1600 sample is greater than that of the SiBN5-1600 sample and that the oxygen content of the oxygen layer is greater than that of the center area. However, EDS analysis reveals that some pores located inside the matrix are clearly visible, which are probably produced during either the initial stage of $B_2O_3$ volatilization or upon the outward diffusion of NO, $NO_2$, and $N_2$ gas due to the oxidation or decomposition of $Si_3N_4$. The boron distribution on the scale was not quantified due to the low sensitivity of SEM/EDS for light elements. The thermodynamic driving force for the formation of boron silicate glass indicates that it restricts $O_2$ inward diffusion and further volatilization of the $B_2O_3$ phase [73,79,80]. Thus, the results indicate that SiBN ceramics with low boron contents are suitable candidate materials with advanced high-temperature oxidation and corrosion resistance.

## 4 Conclusions

In this work, $Si_3N_4$ and SiBN ceramic monoliths were successfully prepared via high-pressure and high-temperature synthesis starting from the corresponding polymer-derived amorphous powders. Advanced characterization revealed that the temperature/pressure ratio and boron content significantly influence the crystallization behavior and phase transformation, as well as the mechanical properties and oxidation behavior. The results revealed that high pressure facilitates the phase transformation from α-$Si_3N_4$ to β-$Si_3N_4$, whereas the presence of boron in $Si_3N_4$ matrix suppresses the phase transformation due to the formation of Si–B–N networks. Moreover, the investigation of the mechanical properties of the resulting samples indicates that SiBN1-derived samples exhibit increased hardness and fracture toughness, which is attributed to the disordered SiBN boundaries enhancing grain boundary sliding by acting as a lubricant. In addition, $Si_3N_4$ ceramics containing moderate amounts of boron (Si:B = 5:1) exhibit remarkable oxidation resistance in comparison to the boron-free $Si_3N_4$ ceramics owing to the formation of borosilicate glass as a protective layer, suggesting potential structural applications of boron-containing $Si_3N_4$ products in high-temperature oxidation and corrosion environments.

### Acknowledgements

Shuailing Ma is grateful for the financial support from the National Natural Science Foundation of China (No. 12204254), the Natural Science Foundation of Zhejiang Province (No. LQ23A040005), and the Program for Science and Technology Innovation Team in Zhejiang (No. 2021R01004). Wei Li acknowledges the career bridge funding support from the Technical University of Darmstadt, Germany. Zhaoju Yu thanks the Natural Science Foundation of China (Nos. 51872246 and 52061135102) for financial support. Marc Widenmeyer and Anke Weidenkaff are grateful for the financial support from the German Ministry of Education and Research (No. 03SF0618B).

### Declaration of competing interest

The authors have no competing interests to declare that are relevant to the content of this article. The author Ralf Riedel is the Advisory Committee of this journal.

### Electronic Supplementary Material

Supplementary material is available in the online version of this article at https://doi.org/10.26599/JAC.2024.9220961.

### References

[1] Bocanegra-Bernal MH, Matovic B. Mechanical properties of silicon nitride-based ceramics and its use in structural applications at high temperatures. *Mat Sci Eng A-Struct* 2010, **527**: 1314–1338.

[2] Krstic Z, Krstic VD. Silicon nitride: The engineering material of the future. *J Mater Sci* 2012, **47**: 535–552.

[3] Tang SJ, Guo WM, Sun SK, *et al.* Design strategy of phase and microstructure of $Si_3N_4$ ceramics with simultaneously high hardness and toughness. *J Adv Ceram* 2023, **12**: 122–131.

[4] Chen HB, Wang WD, Yu X, *et al.* The effect of annealing temperature on flexural strength, dielectric loss and thermal conductivity of $Si_3N_4$ ceramics. *J Alloys Compd* 2020, **813**: 152203.

[5] Zhang J, Liu GH, Cui W, *et al.* Plastic deformation in silicon nitride ceramics via bond switching at coherent interfaces. *Science* 2022, **378**: 371–376.

[6] Liao NB, Xue W, Zhang M. Molecular dynamics investigation of Si–B–N ceramics: Effects of boron content. *Model Simul Mater Sc* 2012, **20**: 035009.

[7] Long X, Shao CW, Wang YD. Effects of boron content on the microwave-transparent property and high-temperature stability of continuous SiBN fibers. *J Am Ceram Soc* 2020, **103**: 4436–4444.

[8] Yan Q, Chen SY, Shi HF, *et al.* Fabrication of polymer-derived SiBCN ceramic temperature sensor with excellent sensing performance. *J Eur Ceram Soc* 2023, **43**: 7373–7380.

[9] Shao G, Jiang JP, Jiang MJ, *et al.* Polymer-derived SiBCN ceramic pressure sensor with excellent sensing performance. *J Adv Ceram* 2020, **9**: 374–379.

[10] Peng GH, Liang M, Liang ZH, *et al.* Spark plasma sintered silicon nitride ceramics with high thermal conductivity using $MgSiN_2$ as additives. *J Am Ceram Soc* 2009, **92**: 2122–2124.

[11] Hampshire S, Silicon nitride ceramics. In: *Engineered Ceramics: Current Status and Future Prospects*. Ohji T, Singh M, Eds. John Wiley & Sons, Inc., 2016: 77–97.

[12] Hirosaki N, Okada A, Matoba K. Sintering of $Si_3N_4$ with the addition of rare-earth oxides. *J Am Ceram Soc* 1988, **71**: 144–147.

[13] Chen SL, Wang L, He G, *et al.* Microstructure and properties of porous $Si_3N_4$ ceramics by gelcasting-self-propagating high-temperature synthesis (SHS). *J Adv Ceram* 2022, **11**: 172–183.

[14] Cinibulk MK, Thomas G, Johnson SM. Grain-boundary-phase crystallization and strength of silicon nitride sintered with a YSiAlON glass. *J Am Ceram Soc* 1990, **73**: 1606–1612.

[15] Cinibulk MK, Thomas G, Johnson SM. Strength and creep behavior of rare-earth disilicate–silicon nitride ceramics. *J Am Ceram Soc* 1992, **75**: 2050–2055.

[16] Rouxel T, Sanglebœuf JC, Huger M, *et al.* Temperature dependence of Young's modulus in $Si_3N_4$-based ceramics: Roles of sintering additives and of SiC-particle content. *Acta Mater* 2002, **50**: 1669–1682.

[17] Wang WD, Yao DX, Liang HQ, *et al.* Effect of the binary nonoxide additives on the densification behavior and thermal conductivity of $Si_3N_4$ ceramics. *J Am Ceram Soc* 2020, **103**: 5891–5899.

[18] Homma K, Okada H, Fujikawa T, *et al.* HIP sintering of silicon nitride without additives. *Int J High Technol Ceram* 1987, **95**: 229–234.

[19] Tanaka I, Pezzotti G, Okamoto T, *et al.* Hot isostatic press sintering and properties of silicon nitride without additives. *J Am Ceram Soc* 1989, **72**: 1656–1660.

[20] Tanaka I, Pezzotti G, Okamoto T, *et al.* Dense silicon nitride without additives: Sintering and high temperature behaviors. In: *A Collection of Papers Presented at the 13th Annual Conference on Composites and Advanced Ceramic Materials: Ceramic Engineering and Science Proceedings*. John B, Wachtman Jr, Eds. Westerville: The American Ceramic Society, Inc., 1989: 817–822.

[21] Lu P, Danforth SC, Symons WT. Microstructure and grain-boundary characterization of HIP'ed high-purity silicon nitride. *J Mater Sci* 1993, **28**: 4217–4222.

[22] Li W, Yu ZJ, Wiehl L, *et al.* Hard and tough novel high-pressure γ-$Si_3N_4$/$Hf_3N_4$ ceramic nanocomposites. *J Adv Ceram* 2023, **12**: 1418–1429.

[23] Lu L, Wen TH, Li W, *et al.* Single-source-precursor synthesis of dense monolithic SiC/$(Ti_{0.25}Zr_{0.25}Hf_{0.25}Ta_{0.25})$C ceramic nanocomposite with excellent high-temperature oxidation resistance. *J Eur Ceram Soc* 2024, **44**: 595–609.

[24] Yang JC, Wen QB, Feng B, *et al.* Microstructural evolution and electromagnetic wave absorbing performance of single-source-precursor-synthesized SiCuCN-based ceramic nanocomposites. *J Adv Ceram* 2023, **12**: 1299–1316.

[25] Munir ZA, Anselmi-Tamburini U, Ohyanagi M. The effect of electric field and pressure on the synthesis and consolidation of materials: A review of the spark plasma sintering method. *J Mater Sci* 2006, **41**: 763–777.

[26] Ilić S, Zec S, Rosić M, *et al.* High pressure densification of nanocrystalline mullite powder. *Ceram Int* 2016, **42**: 5319–5325.
[27] Sun L, Li PH, Ma MD, *et al.* Hard and tough ultrafine-grained $B_4C$–cBN composites prepared by high-pressure sintering. *J Eur Ceram Soc* 2022, **42**: 2015–2020.
[28] Matović B, Maletaškić J, Prikhna T, *et al.* Characterization of $B_4C$–SiC ceramic composites prepared by ultra-high pressure sintering. *J Eur Ceram Soc* 2021, **41**: 4755–4760.
[29] Mashhadi M, Taheri-Nassaj E, Sglavo VM. Pressureless sintering of boron carbide. *Ceram Int* 2010, **36**: 151–159.
[30] Hou ZQ, Wang HK, Yang YN, *et al.* High-pressure synthesis of high-performance submicron-sized polycrystalline β-$Si_3N_4$ bulk without additives. *Ceram Int* 2020, **46**: 12449–12457.
[31] Ma MD, Sun RX, Sun L, *et al.* Enhanced mechanical properties of nanocrystalline $B_4C$–SiC composites by *in situ* high pressure reactive sintering. *J Mater Res Technol* 2023, **27**: 2790–2796.
[32] Dong HF, Li BZ, Liu BB, *et al.* Extraordinary high-temperature mechanical properties in binder-free nanopolycrystalline WC ceramic. *J Mater Sci Technol* 2022, **97**: 169–175.
[33] Ma MD, Sun YN, Wu YJ, *et al.* Nanocrystalline high-entropy carbide ceramics with improved mechanical properties. *J Am Ceram Soc* 2022, **105**: 606–613.
[34] Zhan Y, Li W, Jiang TS, *et al.* Boron-modified perhydropolysilazane towards facile synthesis of amorphous SiBN ceramic with excellent thermal stability. *J Adv Ceram* 2022, **11**: 1104–1116.
[35] Evans AG, Charles EA. Fracture toughness determinations by indentation. *J Am Ceram Soc* 1976, **59**: 371–372.
[36] Schwab ST, Graef RC, Blanchard CR, *et al.* The pyrolytic conversion of perhydropolysilazane into silicon nitride. *Ceram Int* 1998, **24**: 411–414.
[37] Matsunaga K, Iwamoto Y. Molecular dynamics study of atomic structure and diffusion behavior in amorphous silicon nitride containing boron. *J Am Ceram Soc* 2001, **84**: 2213–2219.
[38] Lee DD, Kang SJ L, Petzow G, *et al.* Effect of α to β (β′) phase transition on the sintering of silicon nitride ceramics. *J Am Ceram Soc* 1990, **73**: 767–769.
[39] Rhee SH, Lee JD, Kim DY. Effect of α-$Si_3N_4$ initial powder size on the microstructural evolution and phase transformation during sintering of $Si_3N_4$ ceramics. *J Eur Ceram Soc* 2000, **20**: 1787–1794.
[40] Imamura H, Kawata T, Honda S, *et al.* A facile method to produce rodlike β-$Si_3N_4$ seed crystallites for bimodal structure controlling. *J Am Ceram Soc* 2023, **106**: 1694–1705.
[41] Li W, Widenmeyer M, Ding JX, *et al.* Phase evolution and oxidation resistance of $Si_3N_4$/$HfB_2$/$HfB_xC_yN_{1-x-y}$ ceramic nanocomposites prepared from tailored preceramic polymers. *Ceram Int* 2023, **49**: 34164–34172.
[42] Bocanegra-Bernal MH, Matovic B. Dense and near-net-shape fabrication of $Si_3N_4$ ceramics. *Mat Sci Eng A-Struct* 2009, **500**: 130–149.
[43] Batha HD, Whitney ED. Kinetics and mechanism of the thermal decomposition of $Si_3N_4$. *J Am Ceram Soc* 1973, **56**: 365–369.
[44] Riedel R, Chen IW. *Ceramics Science and Technology: Volume 2: Materials and Properties*. John Wiley & Sons, Inc. 2010.
[45] Zhang JF, Tu R, Goto T. Preparation of Ni-precipitated hBN powder by rotary chemical vapor deposition and its consolidation by spark plasma sintering. *J Alloys Compd* 2010, **502**: 371–375.
[46] Niu ZB, Li DX, Jia DC, *et al.* Comparative study on the microstructure evolution and crystallization behavior of precursor-derived and mechanical alloying derived SiBCN. *J Eur Ceram Soc* 2024, **44**: 668–678.
[47] Baldus HP, Passing G. Studies on SiBN (C)-ceramics: Oxidation- and crystallization behavior lead the way to applications. *MRS Online Proceedings Library (OPL)* 1994, **346**: 617–622.
[48] Kaur S, Mera G, Riedel R, *et al.* Effect of boron incorporation on the phase composition and high-temperature behavior of polymer-derived silicon carbide. *J Eur Ceram Soc* 2016, **36**: 967–977.
[49] Ge KK, Ye L, Han WJ, *et al.* Pyrolysis of polyborosilazane and its conversion into SiBN ceramic. *Adv Appl Ceram* 2014, **113**: 367–371.
[50] Sun LC, Tang YD, Cui Y, *et al.* On the fabrication and mechanical properties of $Si_3N_4$ ceramics with low content sintering additives. *Int J Appl Ceram Tec* 2023, **20**: 1269–1277.
[51] Huang JW, Lv XA, Dong XF, *et al.* Microstructure and mechanical properties of α/β-$Si_3N_4$ composite ceramics with novel ternary additives prepared via spark plasma sintering. *Ceram Int* 2022, **48**: 30376–30383.
[52] Vandeperre LJ, Giuliani F, Lloyd SJ, *et al.* The hardness of silicon and germanium. *Acta Mater* 2007, **55**: 6307–6315.
[53] De Pablos A, Osendi MI, Miranzo P. Correlation between microstructure and toughness of hot pressed $Si_3N_4$ ceramics seeded with β-$Si_3N_4$ particles. *Ceram Int* 2003, **29**: 757–764.
[54] Kawaoka H, Adachi T, Sekino T, *et al.* Effect of α/β phase ratio on microstructure and mechanical properties of silicon nitride ceramics. *J Mater Res* 2001, **16**: 2264–2270.
[55] To T, Stabler C, Ionescu E, *et al.* Elastic properties and fracture toughness of SiOC-based glass–ceramic nanocomposites. *J Am Ceram Soc* 2020, **103**: 491–499.
[56] Kitayama M, Hirao K, Toriyama M, *et al.* High hardness α-$Si_3N_4$ ceramics reinforced by rod-like β-$Si_3N_4$ seed particles. *J Ceram Soc Jpn* 2000, **108**: 646–649.
[57] Lee CH, Lu HH, Wang CA, *et al.* Microstructure and fracture behavior of β-$Si_3N_4$ based nanoceramics. *Ceram Int* 2011, **37**: 641–645.
[58] Li DX, Yang ZH, Jia DC, *et al.* Role of boron addition on phase composition, microstructural evolution and mechanical properties of nanocrystalline SiBCN monoliths. *J Eur Ceram Soc* 2018, **38**: 1179–1189.
[59] Kumar A, Gokhale A, Ghosh S, *et al.* Effect of nano-sized sintering additives on microstructure and mechanical properties of $Si_3N_4$ ceramics. *Mat Sci Eng A-Struct* 2019, **750**: 132–140.
[60] Miyazaki H, Hyuga H, Yoshizawa YI, *et al.* Correlation of wear behavior and indentation fracture resistance in silicon nitride ceramics hot-pressed with alumina and yttria. *J Eur Ceram Soc* 2009, **29**: 1535–1542.
[61] Cao LY, Wang ZH, Yin ZB, *et al.* Investigation on mechanical properties and microstructure of silicon nitride ceramics fabricated by spark plasma sintering. *Mat Sci Eng A-Struct* 2018, **731**: 595–602.
[62] Wang LJ, Qi Q, Cai P, *et al.* New route to improve the fracture toughness and flexural strength of $Si_3N_4$ ceramics by adding $FeSi_2$. *Scripta Mater* 2017, **126**: 11–14.
[63] Chasiotis I, Cho SW, Jonnalagadda K. Fracture toughness and subcritical crack growth in polycrystalline silicon. *J Appl Mech* 2006, **73**: 714–722.
[64] Kovalčíková A, Balko J, Balázsi C, *et al.* Influence of hBN content on mechanical and tribological properties of $Si_3N_4$/BN ceramic composites. *J Eur Ceram Soc* 2014, **34**: 3319–3328.
[65] Decterov SA, Swamy V, Jung IH. Thermodynamic modeling of the $B_2O_3$–$SiO_2$ and $B_2O_3$–$Al_2O_3$ systems. *Int J Mater Res* 2007, **98**: 987–994.
[66] Kumar S, Singh K, Kumar D. $SiO_2$/$B_2O_3$ glass formers effect on transparency and mechanical properties of soda-lime borosilicate glasses for automobile applications. *J Non-Cryst Solids* 2023, **618**: 122530.
[67] Li DX, Yang ZH, Jia DC, *et al.* High-temperature oxidation resistance of dense amorphous boron-rich SiBCN monoliths. *Corros Sci* 2019, **157**: 312–323.
[68] Ziegler G, Kleebe HJ, Motz G, *et al.* Synthesis, microstructure and properties of SiCN ceramics prepared from tailored polymers. *Mater Chem Phys* 1999, **61**: 55–63.

[69] Jin SY, Guo KK, Qi HM, *et al.* High yield polyborosilazane precursor for SiBN ceramics. *Adv Mat Res* 2014, **1004–1005**: 409–414.
[70] Nagano M, Sano H, Sakaguchi S, *et al.* The effect of oxygen addition on oxidation resistance and cutting performance of $Si_3N_4$ ceramics. *Mater Sci Forum* 2007, **534–536**: 1089–1092.
[71] Hirai T, Niihara K, Goto T. Oxidation of CVD $Si_3N_4$ at 1550° to 1650 °C. *J Am Ceram Soc* 1980, **63**: 419–424.
[72] Liang B, Yang ZH, Jia DC, *et al.* Amorphous silicoboron carbonitride monoliths resistant to flowing air up to 1800 °C. *Corros Sci* 2016, **109**: 162–173.
[73] Long X, Wu ZY, Shao CW, *et al.* High-temperature oxidation behavior of SiBN fibers in air. *J Adv Ceram* 2021, **10**: 768–777.
[74] Klemm H. Silicon nitride for high-temperature applications. *J Am Ceram Soc* 2010, **93**: 1501–1522.
[75] Fox DS. Oxidation behavior of chemically-vapor-deposited silicon carbide and silicon nitride from 1200° to 1600 °C. *J Am Ceram Soc* 1998, **81**: 945–950.
[76] Ji SY, Yang J, Liang B, *et al.* Boron-dependent self-healing behavior and mechanical properties of polymer-derived amorphous SiBCN monoliths. *Ceram Int* 2022, **48**: 25326–25334.
[77] Liang B, Zhu QS, Liao XQ, *et al.* Crystallinity dependence of high-temperature oxidation of silicoboron carbonitride monoliths. *Corros Sci* 2021, **187**: 109473.
[78] Du HH, Tressler RE, Spear KE, *et al.* Oxidation studies of crystalline CVD silicon nitride. *J Electrochem Soc* 1989, **136**: 1527–1536.
[79] Sciti D, Brach M, Bellosi A. Long-term oxidation behavior and mechanical strength degradation of a pressurelessly sintered $ZrB_2$–$MoSi_2$ ceramic. *Scripta Mater* 2005, **53**: 1297–1302.
[80] Monteverde F, Bellosi A. Oxidation of $ZrB_2$-based ceramics in dry air. *J Electrochem Soc* 2003, **150**: B552–B559.